The nitrogen isotopic ratio of HC3N towards the L1544 prestellar core

Pierre Hily-Blant, A Faure, C. Vastel, V Magalhaes, B. Lefloch, R. Bachiller

Monthly Notices
of the
ROYAL ASTRONOMICAL SOCIETY

MNRAS **480,** 1174–1186 (2018)
Advance Access publication 2018 June 15

doi:10.1093/mnras/sty1562

The nitrogen isotopic ratio of HC_3N towards the L1544 prestellar core

P. Hily-Blant,[1,2]★ A. Faure,[2]★ C. Vastel,[3] V. Magalhaes,[2] B. Lefloch[2] and R. Bachiller[4]

[1]*Institut Universitaire de France, F-38000 Grenoble, France*
[2]*Université Grenoble Alpes, CNRS, IPAG, F-38000 Grenoble, France*
[3]*IRAP, Université de Toulouse, CNRS, UPS, CNES, F-31400 Toulouse, France*
[4]*Observatorio Astronómico Nacional (OAN, IGN), Calle Alfonso XII 3, E-28014 Madrid, Spain*

Accepted 2018 June 7. Received 2018 June 4; in original form 2018 February 19

ABSTRACT

The origin of the heavily fractionated reservoir of nitrogen in comets remains an issue in the theory of their formation and hence of the Solar system. Whether the fractionated reservoir traced by comets is inherited from the interstellar cloud or is the product of processes taking place in the protostar, or in the protoplanetary disc, remains unclear. So far, observations of nitrogen isotopic ratios in protostars or prestellar cores have not securely identified such a fractionated reservoir owing to the intrinsic difficulty of direct isotopic ratios measurements. In this paper, we report the detection of five rotational lines of HC_3N, including the weaker components of the hyperfine multiplets, and two rotational lines of its ^{15}N isotopologue, towards the L1544 prestellar core. Based on a MCMC/non-LTE multiline analysis at the hyperfine level, we derive the column densities of HC_3N ($8.0 \pm 0.4 \times 10^{13}$ cm^{-2}) and $HC_3^{15}N$ ($2.0 \pm 0.4 \times 10^{11}$ cm^{-2}) and derive an isotopic ratio of $400 \pm 20(1\sigma)$. This value suggests that HC_3N is slightly depleted in ^{15}N in L1544 with respect to the elemental $^{14}N/^{15}N$ ratio of $\approx$330 in the present-day local interstellar medium. Our study also stresses the need for radiative calculations at the hyperfine level. Finally, the comparison of the derived ratio with those obtained in CN and HCN in the same core seems to favour CN+C_2H_2 as the dominant formation route to HC_3N. However, uncertainties in the isotopic ratios preclude definitive conclusions.

Key words: astrochemistry – ISM: individual objects: L1544, L1498, L1527, TMC-1(CP) – ISM: abundances.

1 INTRODUCTION

Isotopic ratios are so far the best tool to follow the volatile content of molecular clouds in their evolution towards the formation of stars, planets, and planetary systems bodies. Observations of sublimating ices from comet 67P/C-G with spectrometers on board the ESA/*ROSETTA* satellite has provided in situ measurements of isotopic ratios of hydrogen, and relative abundances of S_2 and O_2 molecules that consistently support a presolar origin for cometary ices (Altwegg et al. 2015; Rubin et al. 2015; Calmonte et al. 2016). In addition, *Herschel* observations of water towards protostars suggest that less than 10–20 per cent of interstellar ices actually sublimate (van Dishoeck et al. 2014), leaving important amounts of pristine interstellar material available to build up planetary systems. These findings motivate the search for an interstellar heritage within the Solar system while providing insights in the composition of primitive planetary systems in general. Understanding the link between the chemical composition of prestellar and protostellar cores and that of comets, which form at the earliest stages of the planetary formation sequence, is therefore of paramount importance.

Yet, from an observational perspective, measuring isotopic ratios with remote observations is a challenging, and intrinsically time-demanding, task (Taniguchi & Saito 2017). Deriving isotopic ratios generally rests upon several assumptions, some of which being questionable – such as the co-spatial distribution of isotopologues – while others are sometimes difficult to assess – e.g. identical excitation temperatures for the various isotopologues. From interstellar medium standards, the true accuracy is usually larger than the typical 5–10 per cent calibration uncertainties. In contrast, laboratory or in situ measurements of cosmomaterial samples have accuracy at the per cent level (Bonal et al. 2010).

The origin of nitrogen in the Solar system is still an open question. More specifically, the main repository of nitrogen in the protosolar nebula (PSN) is still unclear, although there is some consensus that it may be atomic, N, or molecular, N_2 (Schwarz & Bergin 2014). Furthermore, the large variations of the isotopic ratio of nitrogen ($^{14}N/^{15}N$), as measured in various carriers within different types of Solar system objects, remain unexplained (Aléon 2010; Hily-Blant

★ E-mail: pierre.hily-blant@univ-grenoble-alpes.fr (PH-B); alexandre.faure@univ-grenoble-alpes.fr (AF)

et al. 2013a, 2017; Füri & Marty 2015). One striking problem is the $^{14}N/^{15}N$ isotopic ratio of nitrogen in comets. Its average value, 144 ± 3 (Jehin et al. 2009; Bockelée-Morvan et al. 2015; Shinnaka et al. 2016; Hily-Blant et al. 2017), is three times lower than the bulk ratio of 441 ± 6 in the protosun as inferred from solar wind measurements (Marty et al. 2011). The reasons for these different ratios remain elusive, casting doubts on our understanding of the origin of the composition of comets and more generally of the origin of nitrogen in the Solar system. Several possibilities (not mutually exclusive) could explain the discrepancy: (i) the tracers of nitrogen observed so far in comets – HCN, CN, and NH_2 – are minor reservoirs of cometary nitrogen and thus naturally do not reflect the bulk ratio in the PSN, (ii) efficient fractionation processes in the PSN at the time of comet formation, (iii) efficient fractionation processes in the parent interstellar cloud, and (iv) exchange processes within cometary ices since their formation. Recently, it was shown that protoplanetary discs – or equivalently PSN analogues – carry at least two isotopic reservoirs of nitrogen, traced, respectively, by CN and HCN, with HCN probing a secondary, fractionated, reservoir (Hily-Blant et al. 2017). Furthermore, the isotopic reservoirs traced by HCN and CN are found to be in a 1:3 ratio, respectively, reminiscent of the factor of 3 between the cometary and bulk isotopic ratios (144:441) in the PSN. It follows that exchange processes in parent bodies [possibily (iv) above] are not necessary. The PSN hypothesis is supported by models of selective photodissociation of N_2 in protoplanetary discs (Heays et al. 2014) that predict a strong enrichment of HCN in ^{15}N, but also of CN, in contrast with observations (Hily-Blant et al. 2017). At present, clear-cut observational evidences supporting the PSN or interstellar hypothesis are still lacking.

In this work, we wish to explore the interstellar scenario for the origin of the heavily fractionated cometary nitrogen. From an astrophysical perspective, the main issue is observational, in that the main repositories of nitrogen, N or N_2, are not directly observable in cold interstellar clouds. The bulk isotopic ratio is therefore only measurable indirectly, using the abundances of trace species such as CN or HNC (Adande & Ziurys 2012) and chemical models to infer the bulk. Furthermore, to which extent the isotopic ratio in these trace molecules is actually representative of the bulk depends on their detailed formation pathways, especially molecule-specific fractionation processes that may favour ^{14}N or ^{15}N in those trace species, thus leading to deviations of their isotopic ratios from that of the bulk. In cold and dense clouds, such processes are limited to mass fractionation associated with zero-point energy differences between the two isotopologues (Watson, Anicich & Huntress 1976; Terzieva & Herbst 2000; Heays et al. 2014). Such processes do apply to deuterium and hydrogen, where species such as D_2H+ get enriched by orders of magnitude (Vastel, Phillips & Yoshida 2004). Therefore, to infer the bulk isotopic ratio from trace species, chemical models including detailed fractionation reactions must be used (Terzieva & Herbst 2000; Charnley & Rodgers 2002; Wirström et al. 2012; Hily-Blant et al. 2013b; Roueff, Loison & Hickson 2015; Wirström & Charnley 2018).

To complicate further the inference of isotopic reservoirs in prestellar cores, the derivation of the abundance of the main isotopologue, e.g. CN or HCN, is usually hampered by the large optical depth of the main isotopologue. Hence, double isotopic ratios are used, in which the $[H^{13}CN]/[HC^{15}N]$ abundance ratio is measured, while the $[HCN]/[H^{13}CN]$ abundance ratio is assumed to be equal to the carbon elemental isotopic ratio in the local interstellar medium (ISM), $^{12}C/^{13}C$=68 (Milam et al. 2005). This method has been used intensively, delivering most of the existing nitrogen isotopic ratios in star-forming regions and discs (Adande & Ziurys 2012; Hily-Blant et al. 2013a,b; Wampfler et al. 2014; Guzmán et al. 2017; Zeng et al. 2017; Colzi et al. 2018). However, detailed model calculations (Roueff et al. 2015) have emphasized the pitfalls of the double isotopic ratio method, especially for HCN, suggesting that $[HCN]/[H^{13}CN]$ could be larger than 114, and up to 168, under typical prestellar core conditions. Recent observations in the L1498 prestellar core also emphasized the need for direct measurements, although indicating that the $HCN/H^{13}CN$ ratio is 45 ± 3 (Magalhaes et al. 2018). Isotopic ratios may also be achieved directly in some instances, e.g. with doubly substituted molecules such as NH_2D (Gerin et al. 2009), or with weak hyperfine lines (CN, HCN) at high signal-to-noise ratio (SNR; Adande & Ziurys 2012; Hily-Blant et al. 2017). For other species – N_2H+, NH_3 – direct ratios have been obtained by means of detailed radiative transfer models (Bizzocchi et al. 2013; Lis et al. 2010; Daniel et al. 2013, 2016), although the derivation remains difficult to assess in some cases such as HCN (Daniel et al. 2013).

In this work, we provide a direct measurement of the nitrogen isotopic ratio of the HC_3N cyanopolyyne towards the L1544 prestellar core. This is the first determination of the $^{14}N/^{15}N$ ratio of HC_3N in a prestellar core. The L1544 starless core has been extensively studied (Caselli et al. 2012; Keto, Caselli & Rawlings 2015; Spezzano et al. 2017) and nitrogen isotopic ratios have been obtained in this source, either directly (N_2H+ Bizzocchi et al. 2013) or through double isotopic ratios in HCN or CN (Hily-Blant et al. 2013a,b). The ratio measured in this work is thus compared to that in the chemically related species CN and HCN to derive some clues on the formation route(s) of HC_3N in this source. Our ratio is also put in perspective with that in HC_3N and other species towards different starless cores located in different large-scale environments. We note, in particular, that the first $^{14}N/^{15}N$ ratio of HC_3N was reported only recently by Araki et al. (2016) in the low-mass star-forming region L1527. Even more recently, this ratio was estimated by Taniguchi & Saito (2017) towards the molecular cloud TMC-1 (cyanopolyyne peak, CP), where $HC_5^{15}N$ and DC_7N were also identified (Taniguchi & Saito 2017; Burkhardt et al. 2018).

2 OBSERVATIONS

The observations for all transitions quoted in Table 1 were performed at the IRAM-30m towards the dust peak emission of the L1544 prestellar core ($\alpha_{2000} = 05^h04^m17.21^s$, $\delta_{2000} = 25^\circ10'42.8''$) in the framework of the ASAI Large Program.[1] Observations at frequencies lower than 80 GHz have been performed in December 2015. The EMIR receivers (Carter et al. 2012) were used in combination with the Fast Fourier Transform Spectrometer in its so-called 50 kHz configuration, providing us with 49 kHz spectral resolution, or typically 0.15–0.20 $\mathrm{km\,s^{-1}}$ at the frequency discussed in this paper. Further details on the observations can be found in Vastel et al. (2014) and Quénard et al. (2017). Some, but not all, were observed simultaneously. Nevertheless, the lines were observed within short period of times thus ensuring consistent amplitude calibration throughout the 3 mm band. No other lines of HC_3N or $HC_3^{15}N$ were observed towards L1544 in the frame of the ASAI large programme. The forward and beam efficiencies of the radio-telescope are 0.95 and 0.81, respectively, and all antenna temperatures were brought into the main-beam temperature scale by assuming no spatial dilution, namely $T_{\rm mb} = F_{\rm eff}/B_{\rm eff} \times T_{\rm A}^\star$. Contributions from

[1] Astrochemical Surveys At IRAM: http://www.oan.es/asai

Table 1. Properties of the HC_3N and $HC_3^{15}N$ lines obtained through Gaussian fitting.

Molecule	$J' \rightarrow J$	Rest frequency[a] (GHz)	HPBW (arcsec)	σ_T[b] (mK)	T^c (K)	v_0 ($km\,s^{-1}$)	FWHM ($km\,s^{-1}$)	W^d_{main} (mK $km\,s^{-1}$)	W^d_{hf} (mK $km\,s^{-1}$)	W^d_{tot} (mK $km\,s^{-1}$)
HC_3N	8–7	72.783 82	34	5	3.78	7.22	0.51	2053	88	2141
	9–8	81.881 47	30	5	2.87	7.24	0.53	1633	37	1670
	10–9	90.979 02	27	3	2.66	7.32	0.50	1404	33	1437
	11–10	100.076 39	25	3	1.84	7.23	0.49	956	17	973
	12–11	109.173 63	23	3	1.28	7.22	0.46	626	–	626
$HC_3^{15}N$	9–8	79.500 05	31	6	0.072	7.19	0.18	–	–	14(2)
	10–9	88.333 00	28	2	0.020	7.23	0.42	–	–	9.0(7)
	11–10	97.165 83	25	3	–	–	–	–	–	<1.4
	12–11	105.998 52	23	3	–	–	–	–	–	<1.0
	13–12	114.831 09	21	14	–	–	–	–	–	<4.3

[a]The rest frequency were taken from the CDMS data base.
[b]Statistical uncertainty, at the 1σ level, on the main-beam temperature (in K).
[c]Peak intensity (main beam temperature).
[d]For HC_3N, three integrated intensity values are provided: main component, sum of the two weaker hf lines, and the total (main+hf) flux. For $HC_3^{15}N$, only the main component is detected. The statistical uncertainties (in brackets) are given in units of the last digit at the 1σ level. Upper limits are 1σ.

error-beams where considered negligible for HC_3N. All the following analysis is performed in this T_{mb} scale. The spectra were reduced and analyzed with the CLASS package of the GILDAS software.[2]

3 RESULTS

3.1 Spectra

The HC_3N and $HC_3^{15}N$ spectra are shown in Figs 1 and 2, respectively. The SNR of the HC_3N lines ranges from a few hundreds up to more than a thousand. Indeed, the hyperfine structure of HC_3N has been detected in most cases (see Fig. 1), although only the most widely separated frequencies are resolved leading to essentially three lines instead of 6. The main line thus consists of three overlapping transitions (see Table A1), taking into account that one hf transition is too low to contribute to the emission. Hyperfine lines were also reported for the 5–4 transition of HC_3N towards L1527 (Araki et al. 2016). Table 1 shows that the intensities of the $HC_3^{15}N$ lines are typically 100 times weaker than the main isotopologue, and only two lines ($J = 9-8$ and $10-9$) have been detected.

The observed line properties are summarized in Table 1, including the upper limits on the three undetected $HC_3^{15}N$ lines. The integrated intensities of the three sets of hyperfine lines of HC_3N are given separately in Table A2.

Although our chief objective is to directly determine the isotopic ratio of nitrogen in HC_3N, the physical conditions of the emitting gas must also be known to some extent. One important feature of the present study is the availability of several rotational lines of each isotopologue, which we analyze simultaneously, providing strong constraints on the physical conditions and derived column densities. Furthermore, the critical density of the HC_3N transitions studied here are between 10^5 and $5\times10^5\,cm^{-3}$, which makes them particularly sensitive probes of the density in this, and other, starless cores where the density increases from 10^4 to $10^7\,cm^{-3}$ (Keto et al. 2015).

3.2 Methodology

Our analysis presented below is based on non-local thermodynamic equilibrium (non-LTE) radiative transfer calculations. We have used dedicated collisional rate coefficients for both HC_3N and $HC_3^{15}N$ (Faure, Lique & Wiesenfeld 2016), extended down to 5 K. The collisional partner is restricted to ground-state para-H_2, which dominates at the typical kinetic temperature of 10 K prevailing in such core. For HC_3N, two sets of rates have been used, describing the collisions at the rotational and at the hyperfine levels, respectively. For $HC_3^{15}N$, only the rotational set is needed, assuming identical rate coefficients than for HC_3N. Indeed, substitution of ^{14}N by ^{15}N reduces the rotational constant by only ∼3 per cent while the reduced mass of the collisional system is increased by less than 0.1 per cent. Such changes have a negligible impact on the collisional rate coefficients whose uncertainty is about 10–20 per cent (Faure et al. 2016). The non-LTE radiative transfer calculations were performed using the public code RADEX (van der Tak et al. 2007).

The efficiency of this type of numerical code makes it possible to perform large grids to explore the four-dimensional parameter space (density, kinetic temperature, column densities of both species). Such a frequentist approach allows minima (both local and global) to be found. However, determining uncertainties based on a simple χ^2 approach usually fails because these parameters are indeed not independent from each other but are coupled through the complex interplay of the collisional and radiative excitation processes. In order to explore, and quantify, the correlations between the parameters, we adopted the Markov Chain Monte Carlo (MCMC) approach that enables us to explore the parameter space in a meaningful and efficient way. In practice, we used the emcee PYTHON implementation, an affine invariant sampling algorithm, which is freely available and widely used in the astrophysical community.[3] We also used the corner PYTHON library to produce plots of the parameter distribution and correlation matrix.

In this approach, the parameter space is explored using typically 24 Markov chains for typically 1000–5000 steps, including a burn-in phase of ∼300 steps (see Figs A1 and A2). In our case, the prior probability was a uniform distribution for each parameter, with

[2]http://www.iram.fr/IRAMFR/GILDAS

[3]The code is available at http://dan.iel.fm/emcee.

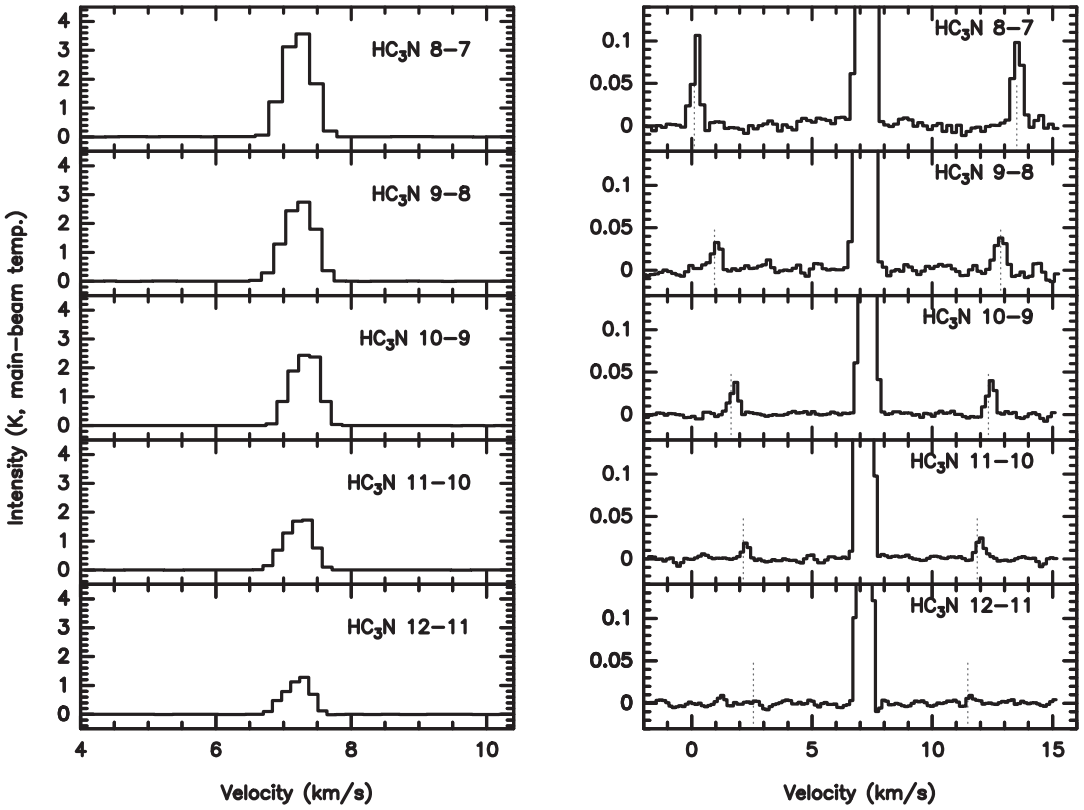

Figure 1. Spectra of HC_3N towards L1544. The scale is magnified in the right panels to show the hyperfine structure.

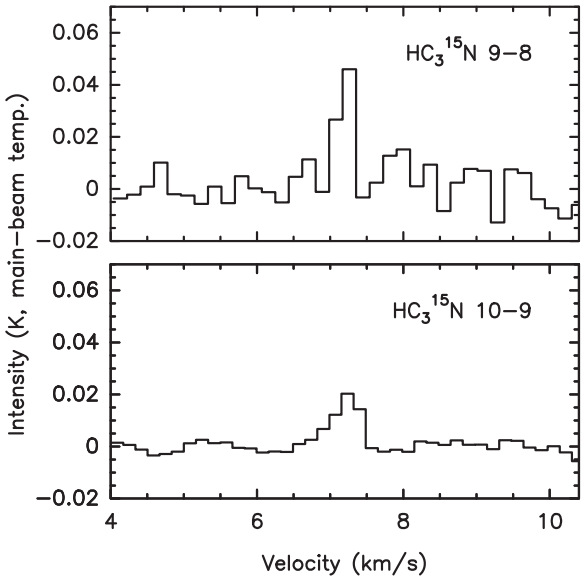

Figure 2. Spectra of the detected $HC_3^{15}N$ lines.

boundaries inferred from physical and chemical considerations. The kinetic temperature T_{kin} varies between 6 and 15 K, while the log10 of the density, HC_3N column density, and isotopic ratio, were taken in the intervals [4: 7], [11: 15], and [2: 3], respectively. This choice ensures that the entire ranges of kinetic temperature and density appropriate to both the envelope and the innermost parts of this core are covered (Keto et al. 2015). The likelihood of each sample was computed as $\exp(-\chi^2)$, with uncertainties on the integrated intensities taken to be at least 5 per cent, significantly larger than the statistical ones obtained from the Gaussian fitting. In performing the MCMC parameter space exploration, the number of chains – also called walkers – and the number of steps of each chain are critically important to ensure that the parameter space has been correctly sampled. It is also important to begin with a physically acceptable solution, although we have successfully tested that various initial conditions lead to the same final distributions. By using multithreading on a four-CPU laptop, the typical execution time was 20 min for 10^5 samples.

3.3 Assumptions

The basic assumption is that both isotopologues are co-spatial, not only in terms of abundance but also in terms of their excitation, such that their emissions come from the same regions within the core. Based on chemical arguments, the two species are expected to be formed by the same pathways, unless specific fractionation routes become efficient. In addition, these two molecules have very similar spectroscopic properties (spontaneous decay and collision rates), and hence are most likely to emit from the same locations in the cloud.

3.4 Physical conditions from the HC_3N lines

3.4.1 Rotational analysis

In a first set of calculations, only the high-SNR HC_3N lines are used to determine the physical conditions. Although the three, unresolved, hf components represent more than 99 per cent of the total intensity (see Table A1), Gaussian fitting of the weaker hf lines

show that they carry 2–4 per cent of the total intensity, thus indicating optical depth effects. The flux predictions based on rotational collisional rate coefficients were thus compared to the total observed flux ($W_{\rm tot}$ in Table 1) of each rotational transition. The results are shown in Fig. 3 and summarized in Table 2 (model labelled 'hc3n-rot'). The corresponding walkers are shown in the Appendix (Fig. A1). As is evident, the five rotational lines do not point towards a single solution but to an ensemble of parameters. Basically, and not surprisingly, the physical conditions are slightly degenerated, with dense gas corresponding to cold temperatures, while warmer gas have lower density. The density is constrained within an order of magnitude, from 10^5 to $10^6\,{\rm cm^{-3}}$, and the kinetic temperature within 7–14 K. In contrast, the column density is relatively well constrained within 0.4 dex, $N({\rm HC_3N}) = 2.0^{+1.2}_{-0.5} \times 10^{13}\,{\rm cm^{-2}}$. This column density agrees well with previous analysis (Quénard et al. 2017). The presently determined physical conditions also confirm those reported by these authors although showing a wider range of solutions.

3.4.2 Hyperfine analysis

A second analysis of the physical conditions of the HC_3N column density was performed in which the flux of each resolved hf line is treated separately. The analysis was conducted using the same tools but with collision rate coefficients at the hyperfine level. The analysis is, however, not as straightforward as in the rotational case because, as already mentioned, three hf transitions, each contributing ≈30 per cent of the total intensity, are not resolved (see Table A1). Thus, to compare the RADEX calculations to the observed flux, the opacity of the three overlapping hf lines were added and the resulting intensity was computed, assuming a single excitation temperature, as

$$W_{\rm main} = [J_\nu(T_{\rm ex}) - J_\nu(2.73)] \times [1 - {\rm e}^{-\sum_k \tau_k}] \times {\rm FWHM} \times 1.064,$$

where the sum runs over the three overlapping lines and $J_\nu = h\nu/k/[\exp(h\nu/kT_{\rm ex}) - 1]$ is the usual radiation temperature function. A Gaussian line profile was adopted, an assumption supported by the opacity of the strongest hf transitions that remains smaller than 0.5 in all models. We also checked that the excitation temperatures of the overlapping hf lines within each rotational transition were effectively equal to within 5 per cent.

The results of the hyperfine analysis are summarized in Table 2 (model labelled 'hc3n-hfs') and shown in Fig. 3. The corresponding walkers are shown in the Appendix (Fig. A1). The correlation between the kinetic temperature and H_2 density is tighter than in the rotational analysis. Kinetic temperatures ranging from 6.5 to 8 K are associated with H_2 densities from 2.5 to 1.0 $\times 10^5\,{\rm cm^{-3}}$, respectively. The physical conditions are therefore consistent with those from the rotational analysis, although with a smaller dispersion around the median values (see Table 2). These kinetic temperatures and densities correspond to the innermost regions of the model of L1544 of Keto et al. (2015). Nevertheless, the derived column density of HC_3N is significantly larger, at the 1σ level, in the hyperfine analysis than from the rotational one, with a value of $(8.0 \pm 0.4) \times 10^{13}\,{\rm cm^{-2}}$. The parameters show similar correlations with each others in both analysis, and in particular, the HC_3N column density increases with the density and decreases with the kinetic temperature.

The excitation temperatures of the best solutions from the rotational analysis are within 7–8 K for all transitions, while somewhat lower values (5–7 K) are obtained from the hyperfine analysis.

3.5 Nitrogen isotopic ratio in HC_3N

To determine the isotopic ratio, the two isotopologues of HC_3N were analyzed simultaneously, using either the total rotational fluxes or the hyperfine fluxes. The upper limits on the $HC_3^{15}N$ lines were taken at the 5σ level, while the uncertainties for the five HC_3N and two $HC_3^{15}N$ detected lines were, as before, at least 5 per cent of the integrated intensity. Several MCMC runs were performed (not shown), with various numbers of steps and initial parameters, to check for parameter space exploration and for convergence towards a consistent set of physical conditions and column densities. The hyperfine analysis was conducted in the same way as before, namely by summing the opacities to compute the flux of the overlapping hyperfine transitions.

The results of the rotational and hyperfine analysis are shown in Fig. 4 and summarized in Table 2 (models all-rot and all-hfs, respectively). The corresponding walkers are shown in the Appendix (Fig. A2). Overall, the parameters show similar correlation patterns as in the previous analysis. In particular, the physical conditions are consistent with the above HC_3N analysis, and the difference between the HC_3N column densities from the rotational and hyperfine analysis is confirmed. The kinetic temperature are $9.4^{+3.4}_{-1.8}$ and $7.2^{+0.3}_{-0.2}$K from the rotational and hf analysis, respectively, and are thus only marginally consistent, whereas the H_2 densities are fully consistent, with the hf analysis resulting in $n({\rm H_2}) = 1.6 \pm 0.3 \times 10^5\,{\rm cm^{-3}}$. The total column density of HC_3N from the hf analysis ($7.8 \pm 0.4 \times 10^{13}\,{\rm cm^{-2}}$) is again significantly larger than from the rotational analysis ($2.0^{+1.3}_{-0.5} \times 10^{13}\,{\rm cm^{-2}}$). These differences translate into the significantly distinct isotopic ratios: the rotational and hyperfine analysis lead to $R = [{\rm HC_3N}]/[{\rm HC_3^{15}N}] = 216 \pm 30$ and 400 ± 20, respectively. The corresponding $HC_3^{15}N$ column densities differ by a factor of 2, being $(9.5^{+9.1}_{-3.4}) \times 10^{10}\,{\rm cm^{-2}}$ and $(19.5^{+1.9}_{-1.7}) \times 10^{10}\,{\rm cm^{-2}}$, respectively.

To compare the two sets of solutions, we computed the hyperfine fluxes associated with the most probable parameters obtained from each analysis (Table 2). These predictions are then compared to the observed fluxes by considering their algebraic distance from the observed flux measured in units of the 1σ rms. The results are shown in Fig. 5. The flux of the strongest hyperfine lines of each rotational line of HC_3N lines are well reproduced, within $\pm 3\sigma$, by both analysis. The fluxes and upper limits of $HC_3^{15}N$ are also well matched. However, the flux of the two weaker hyperfine lines of the 8–7 transition are underpredicted by more than 10σ by the rotational analysis. Similar discrepancies are also found for the 10–9 and 11–10 transitions. In comparison, the hyperfine analysis solution is able to reproduce all fluxes to within $\pm 5\sigma$. The underestimate of the weak, optically thin, hyperfine lines by the rotational analysis directly translates into an underestimate of the column density – despite a larger kinetic temperature – of the main isotopologue, hence, of the isotopic ratio. As is evident, the hyperfine solution is to be preferred.

Another difference between the two analysis is the correlation between $N({\rm HC_3N})$ and R obtained in the rotational fitting but not in the hyperfine analysis (see Fig. 4). Instead, the isotopic ratio presents no clear correlation with any other parameter. This difference suggests that handling separately the hyperfine fluxes adds significant constraints that force the system towards higher HC_3N column densities and removes the low values. Finally, we note that the excitation temperatures are similar to those obtained in the previous analysis of HC_3N only. In particular, the excitation temperatures are close for both isotopologues.

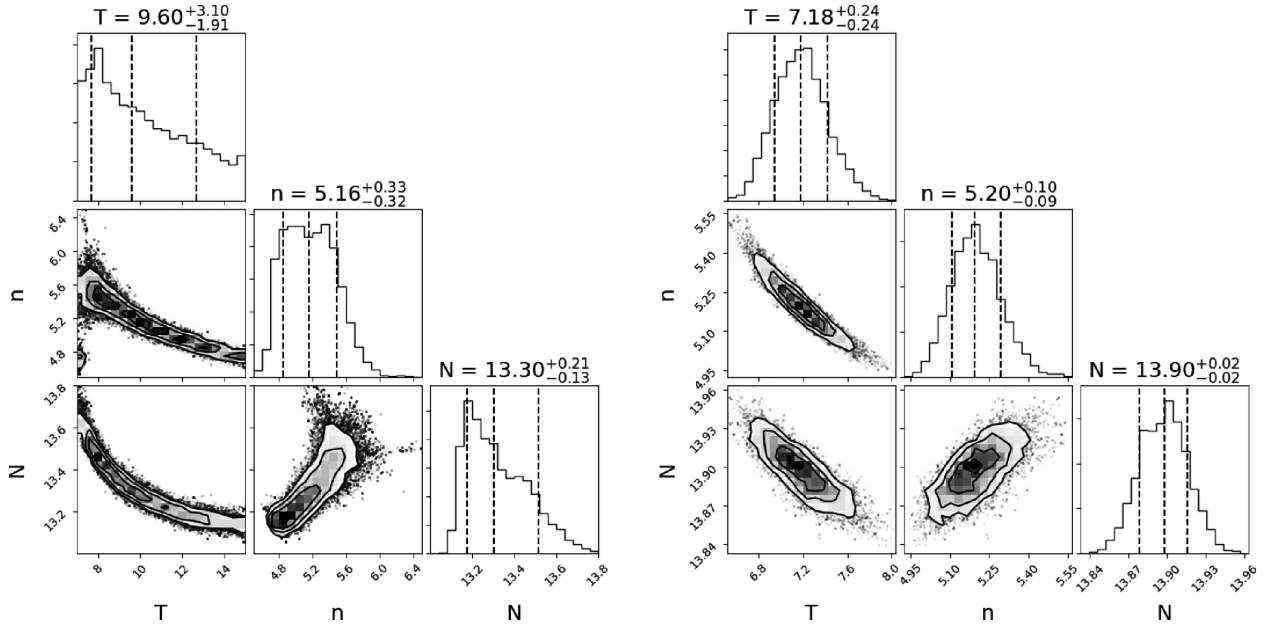

Figure 3. Histograms and cross-histograms from the MCMC parameter space exploration, for the kinetic temperature T, and for the $\log_{10}$ of the density (n) and column density (N) of HC_3N derived from the rotational (left) and hyperfine (right) fluxes (see Table 1 and Section 3.4). In each histogram panel, the median value of the parameter, with the $\pm1\sigma$ boundaries (16 per cent and 84 per cent quantiles), are quoted and indicated by vertical dashed lines (see also Table 2).

Table 2. Results from the MCMC runs applied to the HC_3N and $HC_3^{15}N$ fluxes from Table 1. Results for different number of steps and/or initial conditions are compared.

RunId	Walkers	Steps	Initial conditions[a]				Results[b]			
			T_{kin} (K)	$\log n_{H_2}$ (cm^{-3})	$\log N$ (cm^{-2})	$\log R$	T_{kin} (K)	$\log n_{H_2}$ (cm^{-3})	$\log N$ (cm^{-2})	$\log R$
hc3n-rot[c]	24	5000	8.0	5.0	13.1	–	9.60(−191,+310)	5.16(−32,+33)	13.30(−13,+21)	
hc3n-hfs[c]	24	1000	8.0	5.0	13.1	–	7.18(−24,+24)	5.20(−9,+10)	13.90(−2,+2)	
all-rot[d]	24	5000	8.0	5.6	13.4	2.3	9.44(−183,+339)	5.24(−36,+35)	13.30(−14,+22)	2.32(−5,+ 7)
all-hfs[d]	24	5000	8.0	5.0	13.1	2.2	7.18(−22,+25)	5.19(−9,+ 9)	13.89(−2,+ 2)	2.60(−2,+ 2)

[a] N is the total column density of HC_3N and R is the $[HC_3N]/[HC_3^{15}N]$ abundance ratio.
[b] The median value is given with the 16 per cent and 84 per cent quantiles indicated within brackets in units of the last digit.
[c] Results obtained from the HC_3N lines only, using either the rotational (hc3n-rot) or hyperfine (hc3n-hfs) intensities and the corresponding collision rate coefficients (see also Fig. 3).
[d] Results obtained using both the HC_3N rotational (all-rot) or hf (all-hfs) intensities (see also Fig. 4).

In summary, from our non-LTE hyperfine analysis, the resulting $[HC_3N]/[HC_3^{15}N]$ abundance ratio in L1544 is

$$R = 400 \pm 20.$$

The quoted uncertainty is calculated from the 16 per cent and 84 per cent quantiles (i.e. $\pm1\sigma$) of the resulting distribution as obtained from the MCMC sampling. This uncertainty indeed corresponds to the adopted conservative 5 per cent calibration uncertainty.

4 DISCUSSION

4.1 Nitrogen fractionation in HC_3N

When compared to the elemental ratio of 323 ± 30 in the solar neighbourhood (Hily-Blant et al. 2017), the present direct determination of the $[HC_3N]/[HC_3^{15}N]$ ratio[4] in L1544 shows that HC_3N is, at the 1σ level, slightly depleted in ^{15}N. Recently, the nitrogen isotopic ratio of HC_3N was measured towards the CP in TMC-1 (see Table 3) and a value of 257 ± 54 was obtained (Taniguchi & Saito 2017), not consistent with our present determination. Because both cores are located within the solar neighbourhood, the elemental isotopic ratio of nitrogen should be identical, and different isotopic ratios in L1544 and TMC-1 CP thus indicate different dominant chemical formation pathways in both cores. We note, however, that the TMC1-CP measurement relies on the double isotopic ratio using ^{13}C isotopologues of HC_3N, and a single rotation line ($J = 4 \rightarrow 3$) of $HC_3^{15}N$ is employed.

In the same core, these authors obtained a direct measurement of the HC_5N:$HC_5^{15}N$ abundance ratio that was found to be 323 ± 80, hence indicating no fractionation of nitrogen in this molecule. An indirect measurement by the same authors lead to 344 ± 80. Both measurements thus agree with our value in L1544 for HC_3N to within 1σ uncertainties, which could be interpreted as a signature of common chemical pathways for these two cyanopolyynes, in contrast with the conclusion of these authors. Direct measurement of $^{14}N/^{15}N$ in HC_3N in TMC1-P, using the same kind of approach as the present one, would help clarifying the issue.

The $^{14}N/^{15}N$ isotopic ratio in HC_3N can also be compared to ratios derived in other nitrogen bearing molecules, namely CN, HCN, and N_2H+, in the L1544 prestellar core (Table 3). For CN and

[4] It should be stressed that the isotopic ratios mentioned in what follows are beam averaged measurements.

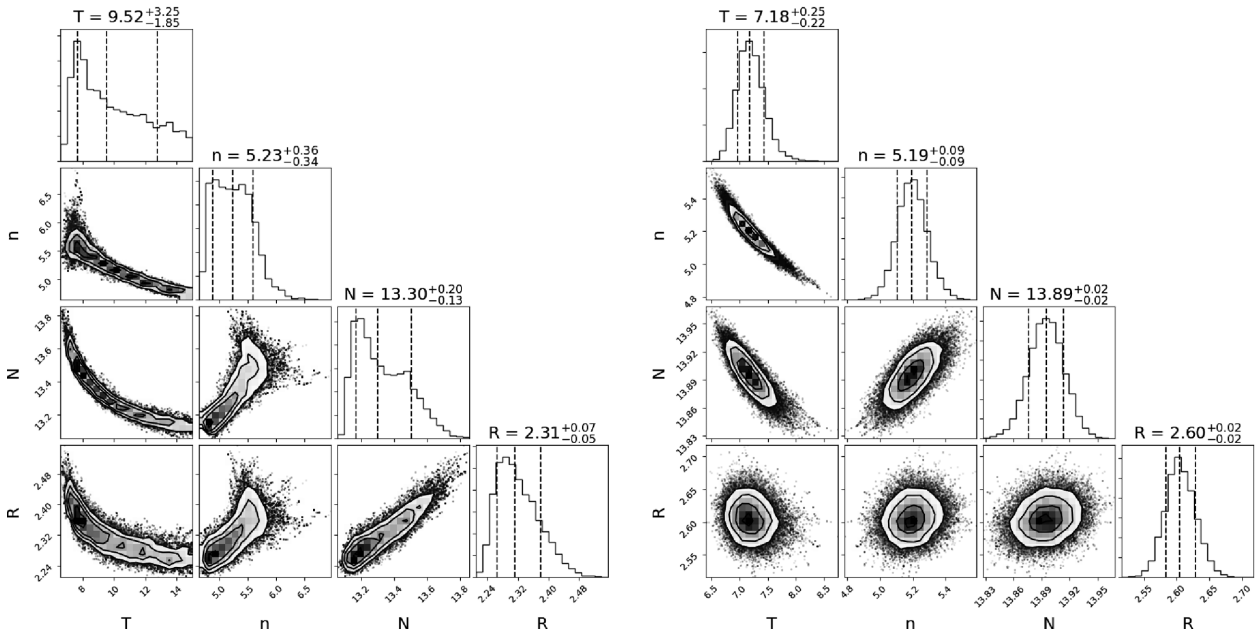

Figure 4. Same as Fig. 3 for the simultaneous analysis of the HC_3N and $HC_3^{15}N$ lines, with R the $\log_{10}$ of the isotopic ratio R. The results are summarized in Table 2. Left: rotational analysis (all-rot model). Right: hyperfine analysis (all-hfs model).

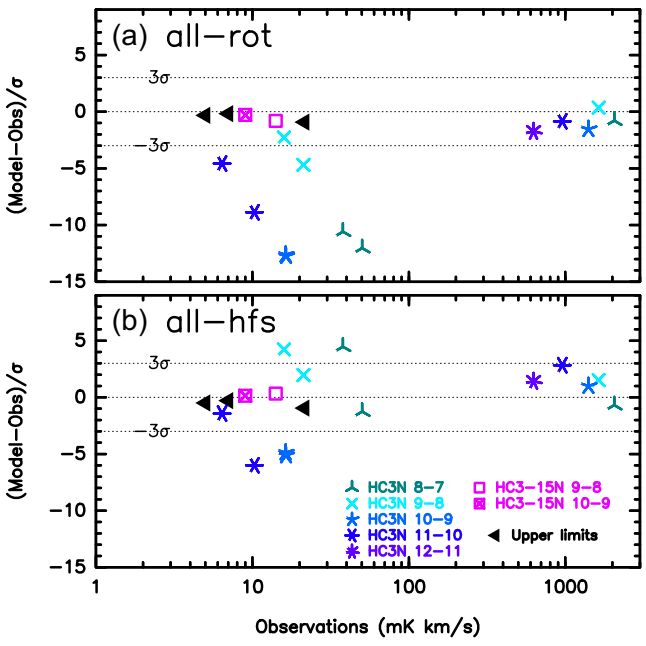

Figure 5. Comparison of the observed and predicted integrated hyperfine intensities (in units of the rms, σ) for the best solutions obtained from the rotational (panel a, all-rot) and hyperfine (panel b, all-hfs) analysis, as reported in Tables 2 and A2. In each panel, the fluxes of the hyperfine components are given for all HC_3N lines except the 12–11 transition for which only the main hf line was detected (see Table 1). The filled triangles indicate the 5σ upper limits on the $HC_3^{15}N$ rotational transitions.

HCN, the ratios were derived indirectly using the double isotopic method, leading to 510 ± 70 for CN and to within 140 to 360 for HCN (Hily-Blant et al. 2013a, b). The present result, $R = 400 \pm 20$, is thus marginally consistent with these values and therefore

Table 3. Compilation of nitrogen isotopic ratios in cyanopolyynes and the directly related species CN and HCN.

Source	Species	R	Method[a]	Reference
TMC1(CP)	HC_3N	270 ± 57	Direct	(1–3)
	HC_3N	257 ± 54	Indirect	(1–2)
	HC_5N	323 ± 80	Direct	(1)
	HC_5N	344 ± 80	Indirect	(1)
L1527	HC_3N	338 ± 12	Indirect	(4)
L1544	HC_3N	400 ± 20	Direct	This work
	HCN	140–350	Indirect	(5)
	CN	500 ± 75	Indirect	(6)
L1498	HCN	338 ± 28	Direct	(7)
	CN	500 ± 75	Indirect	(6)
TW Hya	CN	323 ± 30	Direct	

[a]Direct methods measure the $[X^{15}N]/[X^{14}N]$ abundance ratio; indirect methods use double isotopic ratios.
References: (1) Taniguchi & Saito (2017); (2) Kaifu et al. (2004); (3) Takano et al. (1998); (4) Araki et al. (2016); (5) Hily-Blant et al. (2013a); (6) Hily-Blant et al. (2013b); and (7) Magalhaes et al. (2018)

suggests that CN, HCN, and HC_3N could share a common nitrogen reservoir, as discussed in more detail below. In N_2H+ towards L1544, the ratio is 1000 ± 200, which is also the largest ratio found in any species towards prestellar cores (Hily-Blant et al. 2017). The ratios in N_2H+ and HC_3N are therefore significantly different, at the 3σ level, indicating that they either sample different pools of nitrogen atoms, or that so far unknown fractionation reactions are unevenly partitioning ^{14}N and ^{15}N among these two species.

4.2 Uncertainties

Obtaining reliable and as small as possible uncertainties on column density ratios is certainly one of the main challenges in remote isotopic ratio measurements such as the one presented here.

The statistical uncertainties on the observed HC_3N integrated intensities are extremely small (Table 1). Yet, they hardly reflect the total uncertainty that must take into account the influence of the weather, pointing, focus, and chopper wheel calibration method. At the IRAM-30m telescope, the overall calibration uncertainty is generally taken to be 5 per cent to 10 per cent. Given the fact that all lines in our survey were observed in a consistent way and over a relatively short periods of time, we adopted a flux calibration uncertainty of 5 per cent.

One way to mitigate amplitude calibration uncertainties is to perform simultaneous observations of different lines, which naturally cancel out the multiplicative fluctuations, such as receiver gains. None the less, differential effects across the receiver bandpass remain. Furthermore, it is usually assumed that the main-beam temperature is the appropriate temperature scale, but the true brightness temperature should indeed be derived by convolving the source structure by the complete telescope beam (not only the main beam). Yet, for species such as HC_3N, one does not expect extended, strong, emission, which could contribute significantly through error-beam pickup.

From an observational perspective, it therefore seems extremely difficult to go beyond the calibration-limited accuracy on isotopic ratios. From this regard, our conservative approach differs from that of other authors who propagate the statistical uncertainties (Araki et al. 2016) and claim to reach a 1–2 per cent uncertainty level, despite the use of lines obtained with different telescopes (GBT and NRO).

Furthermore, in addition to the flux calibration, line analysis requires assumptions to be made which carry additional sources of uncertainties – which amount essentially to the assumptions in the radiative transfer – that are usually very difficult to quantify, unless several models can be compared. For instance, the LTE assumption[5] is commonly used to compute column densities from single lines (Hily-Blant et al. 2013a; Araki et al. 2016; Taniguchi & Saito 2017). Although the uncertainty associated with the assumed value of the excitation temperature can be quantified – and is actually generally small when dealing with column density ratios – the uncertainty associated with the LTE assumption itself is much more difficult to estimate. Strictly speaking, the uncertainty on the derived excitation temperature should be propagated into the column densities and column density ratios. Yet, in their analysis, Araki et al. apply the single excitation temperature assumption to the main and ^{13}C isotopologues although the excitation temperatures of the ^{13}C isotopomers differ by up to 20 per cent (see their table 2). Their very small uncertainties on the column density ratios thus neglect the uncertainty associated with their single excitation temperature assumption.

In the present analysis, we have relaxed this assumption by computing non-LTE level populations, at the rotational and hyperfine levels. However, our calculations assume uniform physical conditions although it is clear that assumptions on the source geometry represent an additional source of uncertainties. Indeed, we note that, although the hyperfine fitting provides a much better overall agreement (see Fig. 5), some weak hyperfine components are reproduced only at the 5σ level, which may indicate the limits of our 0D model. The impact of this assumption can only be tested through multidimensional, non-LTE, calculations combined with spectral line mapping observations (Daniel et al. 2013; Magalhaes et al. 2018).

[5]For consistency with the common usage, we use LTE to refer to the assumption of a single (excitation) temperature to describe the level population of a (set of) molecule(s), which is indeed a weaker assumption than that of local thermodynamical equilibrium.

4.3 Formation of HC_3N

The chemistry of HC_3N in dense prestellar cores is still a matter of debate, although it has been studied in great detail especially using carbon isotopic ratios. In particular, ^{13}C isotopic anomalies were observed for HC_3N in the Taurus Molecular Cloud-1 (TMC-1) starless core towards the so-called CP (Takano et al. 1998). The column densities of $H^{13}CCCN$, $HC^{13}CCN$, and $HCC^{13}CN$ follow the ratios 1.0:1.0:1.4, respectively, which was interpreted as a result of the production pathway of HC_3N rather than isotope exchange reactions. The latter are unlikely because the zero-point energy differences between the three carbon isotopologues would not predict $[H^{13}CCCN]/[HC^{13}CCN]$ close to 1. Instead, HC_3N is thought to form primarily from a parent molecule having two equivalent carbon atoms in order to explain $[H^{13}CCCN] = [HC^{13}CCN]$. Currently, three potential formation routes are considered, through CN, HCN, and HNC (for a review, see e.g. Taniguchi, Saito & Ozeki 2016).

4.3.1 The HCN *route*

In this route, the two equivalent carbons are provided by C_2H_2+:

$$C_2H_2 + +HCN \rightarrow HC_3NH + +H. \quad (1)$$

This reaction is known to be rapid at room temperature with a rate coefficient $k_1 = 3.78 \times 10^{-11}$ cm^3 s^{-1} (Iraqi et al. 1990). This reaction is followed by the dissociative recombination (DR) between HC_3NH+ and electrons. The branching ratios of this DR process have not been measured for each product channel (Vigren et al. 2012), but quantum calculations indicate that all isomers of HC_3N, namely HNC_3, HCCNC, and HCNCC can be produced at low temperature. In particular, if reaction (1) is a major pathway to produce HC_3N, then HC_3N and HNC_3 are expected to have similar abundances since both products result from a direct hydrogen elimination of the parent ion HC_3NH+ (Osamura et al. 1999). The observation of HC_3N and its isomers HCCNC and HNC_3, however, indicates that the three species have very different abundances in the cold conditions of TMC-1 (Ohishi & Kaifu 1998) as well as in L1544 (Vastel et al. 2018). Assuming that HC_3N and HNC_3 have a similar reactivity, this suggests that reaction (1) is not a major pathway to HC_3N (see the discussion in Vastel et al. 2018).

4.3.2 The CN route

Here, the two equivalent carbons come from C_2H_2:

$$C_2H_2 + CN \rightarrow HC_3N + H. \quad (2)$$

This reaction is also rapid at room temperature with a rate coefficient $k_2 = 2.5 \times 10^{-10}$ cm^3 s^{-1} (Sims et al. 1993). Reaction (2) has even been found to accelerate down to 25 K (Sims et al. 1993). The current consensus is that HC_3N is mainly produced through the neutral–neutral reaction (2). In addition, the larger abundance of $HCC^{13}CN$ relative to $H^{13}CCCN$ and $HC^{13}CCN$ can be easily explained by different $^{12}C/^{13}C$ isotopic ratios in C_2H_2 and CN, since the triple –CN bond is conserved in reaction (2). This scenario has been recently supported by observations of $H^{13}CCCN$, $HC^{13}CCN$, $HCC^{13}CN$, and HC_3N towards the L1527 protostar, which were found to follow the ratios 1.00:1.01:1.35:86.4, respectively (Araki et al. 2016). This corresponds to a $^{12}C/^{13}C$ isotopic ratio of 64

for [HCC^{13}CN]/[HC$_3$N], in good agreement with the local ISM elemental ^{12}C/^{13}C ratio of 68 (Milam et al. 2005). This, in turn, seems to indicate that CN is not fractionated in carbon. Furthermore, the significantly higher ^{12}C/^{13}C ratios in H^{13}CCCN and HC^{13}CCN of ≈86 is consistent with ^{13}C depletion in C_2H_2, as observed in other carbon-chain molecules (see Roueff et al. 2015; Araki et al. 2016, and references therein).

In the L1527 protostar, Araki et al. (2016) also determined a [HCC^{13}CN]/[HC$_3^{15}$N] abundance ratio of 5.26 ± 0.19, resulting in a [HC$_3$N]/[HC$_3^{15}$N] ratio of 338 ± 12. This value is again close to the elemental ^{14}N/^{15}N ratio in the local ISM (Adande & Ziurys 2012; Hily-Blant et al. 2017). To our knowledge, the ^{12}C/^{13}C and ^{14}N/^{15}N ratios in CN in L1527 are unknown so that a firm conclusion regarding the link between CN and HC$_3$N cannot be established in this source.

4.3.3 The HNC route

The third route, with three non-equivalent carbon atoms, is

$$\mathrm{HNC} + \mathrm{C_2H} \rightarrow \mathrm{HC_3N} + \mathrm{H}. \quad (3)$$

The rate coefficient is unknown, but the *ab initio* computations of Fukuzawa & Osamura (1997) have shown that this reaction is exothermic with no energy barrier. A rate coefficient of $k_3 = 1.75 \times 10^{-10}$ cm^3 s^{-1} was suggested by Hébrard et al. (2012). In reaction (3), the H atom is removed from HNC, and we thus expect [H^{13}CCCN]/[HC^{13}CCN] = [C^{13}CH]/[^{13}CCH] at odds with the observations towards TMC-1 and L1527 that find [C^{13}CH]/[^{13}CCH] abundance ratios of ∼1.6 (Sakai et al. 2010). The origin of the departure of [C^{13}CH]/[^{13}CCH] from unity is likely associated with the neutral–neutral fractionation reaction ^{13}CCH + H → C^{13}CH + H + 8.1K. Indeed, at a kinetic temperature of 15 K, the equilibrium abundance ratio due to this reaction is exp (8.1/15) = 1.7, which is in harmony with the observed ratios. At the lower temperature of TMC-1 (CP), where the steady-state ratio would be 2.2, chemical model calculations show that the 1.6 ± 0.4(3σ) ratio can be obtained at early times, when carbon is still mostly neutral (Furuya et al. 2011). As a consequence of the different [H^{13}CCCN]/[HC^{13}CCN] and [C^{13}CH]/[^{13}CCH] abundance ratios, the HNC route was discarded by Taniguchi et al. (2016).

However, recently, the [H^{13}CCCN]/[HC^{13}CCN] abundance ratio was measured towards two cold prestellar cores, L1521B and L134N, with values of 0.98 ± 0.14 and 1.5 ± 0.2 (1σ uncertainties), respectively, suggesting different formation pathways for HC$_3$N in these two sources (Taniguchi, Ozeki & Saito 2017). In particular, the ratio in L134N could indicate that HC$_3$N is primarily formed from HNC + C$_2$H, while CN + C_2H_2 would be the main route in L1521B, as in TMC-1(CP) and L1527 (Takano et al. 1998; Araki et al. 2016). The competition between the CN and HNC routes was interpreted by Taniguchi et al. (2017) as reflecting different [CN]/[HNC] abundance ratios in the two prestellar cores L1521B and L134N. Observations of the [C^{13}CH]/[^{13}CCH] in both sources should bring valuable information.

4.3.4 Consequences of the nitrogen isotopic ratio of HC$_3$N

The present determination of the [HC$_3$N]/[HC$_3^{15}$N] ratio in L1544 brings a new piece of the HC$_3$N puzzle. The [CN]/[C^{15}N] abundance ratio in this source is 510 ± 70, as obtained using a non-LTE hyperfine analysis and assuming a [CN]/[^{13}CN] ratio of 68 (Hily-Blant et al. 2013b). The ^{14}N/^{15}N ratio in HC$_3$N is thus consistent with the [CN]/[C^{15}N] ratio in L1544 to within 1.5σ.

On the other hand, [HCN]/[HC^{15}N] = 257± 30 was measured at the central position of L1544, again using a non-LTE hyperfine analysis and assuming a value of 68 for the [HCN]/[H^{13}CN] ratio (Hily-Blant et al. 2013a). The ^{14}N/^{15}N ratio in HC$_3$N is thus not consistent with that of [HCN]/[HC^{15}N] in L1544, which would exclude the HCN route, in agreement with the HC$_3$N isomer abundances discussed above. We note, however, that the uncertainties introduced by the double isotopic method (for both CN and HCN) are certainly larger than the above quoted error bars. Finally, to our knowledge, no measurement of ^{14}N/^{15}N in HNC has been reported so far in L1544. It is therefore not possible to conclude with certainty about the main production pathway of HC$_3$N in L1544: each of the three above routes (from HCN, CN, and HNC) might indeed contribute to the derived ^{14}N/^{15}N ratio of 400. The HCN route is, however, very likely a minor pathway.

4.4 Fractionation of nitrogen in prestellar cores

Our [HC$_3$N]/[HC$_3^{15}$N] abundance ratio of 400 suggests that HC$_3$N is only slightly depleted in ^{15}N with respect to the elemental ratio of ≈330 in the solar neighbourhood.

Models of nitrogen chemical fractionation have been developed and applied to dense gas, from the typical 10^4 cm^{-3} of prestellar clouds where mild effects are predicted (Terzieva & Herbst 2000), to the much higher density, 10^7 cm^{-3}, of protostars (Charnley & Rodgers 2002; Wirström & Charnley 2018) where high degrees of fractionation are promoted by the heavy depletion of carbon monoxide. More recently, the set of fractionation reactions was revised (Roueff et al. 2015), and the dominant fractionation routes were disqualified on energetic grounds. Accordingly, these models predict that the steady-state isotopic ratios of all trace species should reflect the elemental ratio. Regardless of the detailed formation pathway of HC$_3$N, our new direct measurement thus seems to support these model predictions. However, the current understanding of nitrogen chemical fractionation is still not well established. Indeed, chemical calculations using the fractionation network of Terzieva & Herbst (2000) in combination with the chemical network of Hily-Blant et al. (2010) predict significant variations of the isotopic ratios for most of the observable nitrogenated species, especially HCN (Hily-Blant et al. 2013b). Moreover, the isotopic ratio measured directly in N_2H+ is ≈1000 in the L1544 core, suggesting strong depletion in ^{15}N (Bizzocchi et al. 2013) which no model is able to reproduce. Finally, we note that the recent models of Roueff et al. also predict that carbon fractionation would lead to HCN/H^{13}CN ratio up to ∼140, in sharp contrast with the value of 45 ± 3 obtained recently in the L1498 prestellar core (Magalhaes et al. 2018). Therefore, putting these model predictions on a firmer ground requires further observations not only to accurately measure isotopic ratios but also to test the chemical fractionation models.

5 CONCLUDING REMARKS

Molecular isotopic ratios are invaluable tools for studying the origin of the Solar system and the possible link between the primordial matter and interstellar chemistry. As discussed above, they also offer powerful diagnostics to reveal the underlying chemistry. We have derived the first ^{14}N/^{15}N ratio of HC$_3$N in a prestellar core, L1544. This ratio, $R = 400 \pm 20$, is consistent with that derived in the same source for CN (510 ± 70) but significantly larger than the

ratio derived indirectly for HCN (257 ± 30). As such, the present observations seem to favour the $CN + C_2H_2$ route as the major pathway to HC_3N. A similar conclusion was also reached by Vastel et al. (2018) based on the relative abundances of the HC_3N isomers.

From a chemical modelling perspective, two important issues must be addressed. One is the discrepancy with the observations regarding the $^{12}C/^{13}C$ in HCN, which may be related to incorrect fractionation routes, or to the chemistry of nitriles itself. The other is the $^{14}N/^{15}N$ ratio in N_2H+. At this point, it must be emphasized that observational constraints to fractionation models are provided in terms of the comparison of the measured isotopic ratios in a given species against the elemental ratio. The elemental ratio is known to vary with time and with the galactocentric distance (Adande & Ziurys 2012; Romano et al. 2017; Colzi et al. 2018). The value of the elemental $^{14}N/^{15}N$ ratio in the local ISM, at ≈8 kpc, to which measurements in the local ISM, such as the present $HC_3N/HC_3^{15}N$ ratio should be compared, is expected to be lower than its value in the PSN, 4.6 Gyr ago, based on galactic chemical evolution model predictions (Romano et al. 2017). A new value of this ratio, ≈330, was indeed proposed for the present-day solar neighbourhood (Hily-Blant et al. 2017), based on the compilation of direct measurements obtained in the dense, local ISM. This value also agrees very well with the model predictions (Romano et al. 2017). In addition, new measurements have been published recently that are in very good agreement with this elemental ratio (Taniguchi & Saito 2017; Kahane et al. 2018; Magalhaes et al. 2018). Because chemical mass fractionation decreases with temperature, observations of warm gas provide more direct probes of the bulk ratio in the present-day local ISM.

From an observational perspective, it is still necessary to disentangle between the different precursors of HC_3N. In particular, the measurement of the $^{12}C/^{13}C$ ratios in the three ^{13}C isotopomers of HC_3N would provide a crucial test of the CN versus HNC routes. The determination of the $^{14}N/^{15}N$ ratio in HC_3NH+ would also be decisive to definitively exclude the HCN route. We note that the main isotopologue, HC_3NH+, has been observed recently in L1544 (Quénard et al. 2017).

More generally, further observations and radiative transfer calculations are required to put robust constraints on the $^{14}N/^{15}N$ isotopic ratio in various species, including hydrides and nitriles, in L1544 and similar prestellar cores. In particular, future works should revisit the $^{14}N/^{15}N$ in CN and HCN in the L1544 (and other) cores, as recently done in L1498 (Magalhaes et al. 2018). In this context, we emphasize that future isotopic ratios should be determined with a methodology similar to the one presented in this work, i.e. a non-LTE analysis combined with a robust statistical approach in order to control, and minimize, the uncertainties. Moreover, the present work demonstrates the large, non-statistical, uncertainties resulting from using a rotational analysis. This stresses the need for collision rate coefficients at the hyperfine level. Ideally, hyperfine overlap must be taken into account, as was recently demonstrated for HCN in L1498 Magalhaes et al. (2018).

ACKNOWLEDGEMENTS

This study is based on observations from the IRAM/ASAI large programme. We thank the anonymous referee for a careful reading and general comments that helped to improve the manuscript. We wish to thank Martin Legrand and Luc Lefort who participated into the multiline analysis and the implementation of the MCMC/Radex code during their internship in our group in 2017 May–July. PHB acknowledges the *Institut Universitaire de France* for financial support. AF acknowledges the financial support from the CNRS Programme National PCMI (Physique et Chimie du Milieu Interstellaire).

REFERENCES

Adande G. R., Ziurys L. M., 2012, ApJ, 744, 194
Aléon J., 2010, ApJ, 722, 1342
Altwegg K. et al., 2015, Science, 347
Araki M., Takano S., Sakai N., Yamamoto S., Oyama T., Kuze N., Tsukiyama K., 2016, ApJ, 833, 291
Bizzocchi L., Caselli P., Leonardo E., Dore L., 2013, A&A, 555, A109
Bockelée-Morvan D. et al., 2015, Space Sci. Rev., 197, 47
Bonal L., Huss G. R., Krot A. N., Nagashima K., Ishii H. A., Bradley J. P., 2010, Geochim. Cosmochim. Acta, 74, 6590
Burkhardt A. M., Herbst E., Kalenskii S. V., McCarthy M. C., Remijan A. J., McGuire B. A., 2018, MNRAS, 474, 5068
Calmonte U. et al., 2016, MNRAS, 462, S253
Carter M. et al., 2012, A&A, 538, A89
Caselli P. et al., 2012, ApJ, 759, L37
Charnley S. B., Rodgers S. D., 2002, ApJ, 569, L133
Colzi L., Fontani F., Caselli P., Ceccarelli C., Hily-Blant P., Bizzocchi L., 2018, A&A, 609, A129
Daniel F. et al., 2013, A&A, 560, A3
Daniel F. et al., 2016, A&A, 592, A45
Faure A., Lique F., Wiesenfeld L., 2016, MNRAS, 460, 2103
Fukuzawa K., Osamura Y., 1997, ApJ, 489, 113
Füri E., Marty B., 2015, Nature Geosc., 8, 515
Furuya K., Aikawa Y., Sakai N., Yamamoto S., 2011, ApJ, 731, 38
Gerin M., Marcelino N., Biver N., Roueff E., Coudert L. H., Elkeurti M., Lis D. C., Bockelée-Morvan D., 2009, A&A, 498, L9
Guzmán V. V., Öberg K. I., Huang J., Loomis R., Qi C., 2017, ApJ, 836, 30
Heays A. N., Visser R., Gredel R., Ubachs W., Lewis B. R., Gibson S. T., van Dishoeck E. F., 2014, A&A, 562, A61
Hébrard E., Dobrijevic M., Loison J. C., Bergeat A., Hickson K. M., 2012, A&A, 541, A21
Hily-Blant P., Walmsley M., Pineau des Forêts G., Flower D., 2010, A&A, 513, A41
Hily-Blant P., Bonal L., Faure A., Quirico E., 2013a, Icarus, 223, 582
Hily-Blant P., Pineau des Forêts G., Faure A., Le Gal R., Padovani M., 2013b, A&A, 557, A65
Hily-Blant P., Magalhaes V., Kastner J., Faure A., Forveille T., Qi C., 2017, A&A, 603, L6
Iraqi M., Petrank A., Peres M., Lifshitz C., 1990, Int. J. Mass Spectrom. Ion Process., 100, 679
Jehin E., Manfroid J., Hutsemékers D., Arpigny C., Zucconi J.-M., 2009, Earth Moon Planets, 105, 167
Kahane C., Jaber Al-Edhari A., Ceccarelli C., López-Sepulcre A., Fontani F., Kama M., 2018, ApJ, 852, 130
Kaifu N. et al., 2004, PASJ, 56, 69
Keto E., Caselli P., Rawlings J., 2015, MNRAS, 446, 3731
Lis D. C., Wootten A., Gerin M., Roueff E., 2010, ApJ, 710, L49
Magalhaes V., Hily-Blant P., Faure A., Hernandez-Vera M., Lique F., 2018, A&A in press
Marty B., Chaussidon M., Wiens R. C., Jurewicz A. J. G., Burnett D. S., 2011, Science, 332, 1533
Milam S. N., Savage C., Brewster M. A., Ziurys L. M., Wyckoff S., 2005, ApJ, 634, 1126
Ohishi M., Kaifu N., 1998, Faraday Discuss., 109, 205
Osamura Y., Fukuzawa K., Terzieva R., Herbst E., 1999, ApJ, 519, 697
Quénard D., Vastel C., Ceccarelli C., Hily-Blant P., Lefloch B., Bachiller R., 2017, MNRAS, 470, 3194
Romano D., Matteucci F., Zhang Z.-Y., Papadopoulos P. P., Ivison R. J., 2017, MNRAS, 470, 401
Roueff E., Loison J. C., Hickson K. M., 2015, A&A, 576, A99
Rubin M. et al., 2015, Science, 348, 232

Sakai N., Saruwatari O., Sakai T., Takano S., Yamamoto S., 2010, A&A, 512, A31
Schwarz K. R., Bergin E. A., 2014, ApJ, 797, 113
Shinnaka Y., Kawakita H., Jehin E., Decock A., Hutsemékers D., Manfroid J., Arai A., 2016, MNRAS, 462, S195
Sims I. R., Queffelec J.-L., Travers D., Rowe B. R., Herbert L. B., Karthäuser J., Smith I. W. M., 1993, Chemical Physics Letters, 211, 461
Spezzano S., Caselli P., Bizzocchi L., Giuliano B. M., Lattanzi V., 2017, A&A, 606, A82
Takano S. et al., 1998, A&A, 329, 1156
Taniguchi K., Saito M., 2017, Publ. Astron. Soc. Japan, 69, L7
Taniguchi K., Saito M., Ozeki H., 2016, ApJ, 830, 106
Taniguchi K., Ozeki H., Saito M., 2017, ApJ, 846, 46
Terzieva R., Herbst E., 2000, MNRAS, 317, 563
van der Tak F. F. S., Black J. H., Schöier F. L., Jansen D. J., van Dishoeck E. F., 2007, A&A, 468, 627
van Dishoeck E. F., Bergin E. A., Lis D. C., Lunine J. I., 2014, Water: From Clouds to Planets, University of Arizona Press. p. 835
Vastel C., Phillips T. G., Yoshida H., 2004, ApJ, 606, L127
Vastel C., Ceccarelli C., Lefloch B., Bachiller R., 2014, ApJ, 795, L2
Vastel C., Kawaguchi K., Quénard D., Ohishi M., Lefloch B., Bachiller R., Müller H. S. P., 2018, MNRAS, 474, L76
Vigren E. et al., 2012, ApJ, 757, 34
Wampfler S. F., Jørgensen J. K., Bizzarro M., Bisschop S. E., 2014, A&A, 572, A24
Watson W. D., Anicich V. G., Huntress W. T., 1976, ApJ, 205, L165
Wirström E. S., Charnley S. B., 2018, MNRAS, 474, 3720
Wirström E. S., Charnley S. B., Cordiner M. A., Milam S. N., 2012, ApJ, 757, L11
Zeng S. et al., 2017, A&A, 603, A22

APPENDIX: RADEX/MCMC CALCULATIONS

The walkers, or chains, in our rotational and hyperfine analysis of the HC_3N lines are shown in Fig. A1. As can be seen, a good convergence and parameter space exploration is obtained, especially for the hyperfine analysis. Similar plots for the study of the isotopic ratio are shown in Fig. A2. Note that the prior probabilities are uniform for each parameter, within 6–15 K for the kinetic temperature, 10^4–10^{12} cm^{-3} for the H_2 density, and 10^{12}–10^{15} cm^{-2} for the column density of HC_3N. The hyperfine structure of HC_3N is detailed in Table A1, where of the 6 hf transitions within each rotational multiplet, only 5 are listed.

A1 Physical conditions

The predicted flux and flux ratios corresponding to our best models are summarized in Table A2 and shown in Fig. 5.

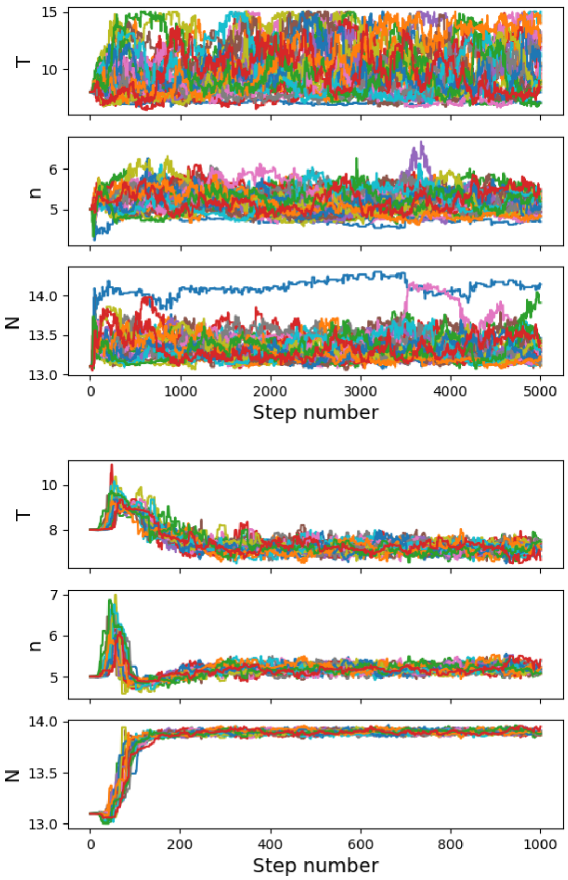

Figure A1. The 24 walkers along their 5000 and 1000 steps evolution associated with the rotational and hyperfine analysis (resp.) of the HC_3N lines (see Fig. 3 and Table 2).

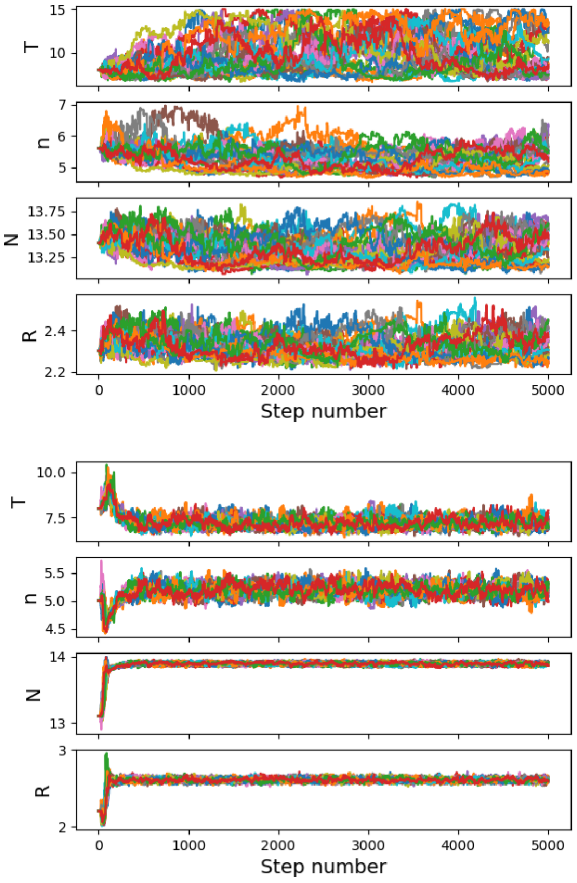

Figure A2. Markov chains of the runs used to measure the nitrogen isotopic ratio of HC_3N (see Table 2). *Top:* all-rot results. *Bottom:* all-hfs results. For the sake of clarity, the legends do not specify that the density and column density are on a log10 scale. Note that the prior probabilities are uniform for each parameter, within 6–15 K for the temperature, 10^4–10^{12} cm^{-3} for the H_2 density, and 10^{12}–10^{15} cm^{-2} for the column density of HC_3N.

Table A1. Theoretical relative intensities of the various hf components of each rotational multiplet of HC_3N.

$N \rightarrow N'^a$	$F \rightarrow F'^a$	Frequency (MHz)	A_{ul}^b (s^{-1})	RI^c (per cent)
8–7	8–8	72.782 29	4.60E−07	0.52
8–7	7–6	72.783 81	2.89E−05	28.89
8–7	8–7	72.783 82	2.90E−05	32.85
8–7	9–8	72.783 83	2.94E−05	37.22
8–7	7–8	72.784 01	2.04E−09	0.00
8–7	7–7	72.785 54	5.21E−07	0.52
9–8	9–9	81.879 92	5.20E−07	0.41
9–8	8–7	81.881 45	4.16E−05	29.42
9–8	9–8	81.881 47	4.16E−05	32.88
9–8	10–9	81.881 48	4.22E−05	36.87
9–8	8–9	81.881 63	1.80E−09	0.00
9–8	8–8	81.883 17	5.82E−07	0.41
10–9	10–10	90.977 44	5.81E−07	0.33
10–9	9–8	90.978 98	5.75E−05	29.84
10–9	10–9	90.978 99	5.75E−05	32.99
10–9	11–10	90.979 00	5.81E−05	36.50
10–9	9–10	90.979 14	1.61E−09	0.00
10–9	9–9	90.980 69	6.42E−07	0.33
11–10	11–11	100.074 83	6.42E−07	0.28
11–10	10–9	100.076 38	7.70E−05	30.15
11–10	11–10	100.076 39	7.71E−05	33.07
11–10	12–11	100.076 40	7.77E−05	36.22
11–10	10–11	100.076 52	1.46E−09	0.00
11–10	10–10	100.078 08	7.03E−07	0.28
12–11	12–12	109.172 08	7.03E−07	0.23
12–11	12–11	109.173 64	1.01E−04	33.28
12–11	11–10	109.173 64	1.00E−04	30.31
12–11	13–12	109.173 65	1.01E−04	35.94
12–11	11–11	109.175 32	7.64E−07	0.23

[a]N is the rotational quantum number, $F = N$, $N \pm I$ identifies the hyperfine sublevels, and $I = 1$ is the nuclear spin of the ^{14}N atom.
[b]Hyperfine Einstein coefficient for spontaneous decay.
[c]Normalized relative intensities in per cent.

Table A2. Model predictions for the most probable solutions from the rotational and hyperfine (fluxes and flux ratios) analysis.

Species	Transition[a]	Observations[b]		all-rot[c]		all-hfs[c]	
		W	σ	$\widetilde{W}$	$\lvert\widetilde{W}-W\rvert/\sigma$	$\widetilde{W}$	$\lvert\widetilde{W}-W\rvert/\sigma$
HC_3N	8–7	37.9	1.9	17.8	−10.6	46.4	4.5
		2053.0	102.7	1971.3	−0.8	1982.4	−0.7
		50.3	2.7	17.8	−12.1	46.9	−1.3
	9–8	15.9	2.2	10.9	−2.3	25.2	4.2
		1633.0	81.7	1662.4	0.4	1756.9	1.5
		21.2	2.2	10.9	−4.7	25.5	2.0
	10–9	16.4	0.8	6.2	−12.5	12.3	−5.0
		1404.0	70.2	1295.9	−1.5	1474.3	1.0
		16.3	0.8	6.2	−12.4	12.4	−4.7
	11–10	6.4	0.7	3.2	−4.5	5.4	−1.4
		956.2	47.8	915.6	−0.8	1091.6	2.8
		10.3	0.8	3.2	−9.0	5.5	−6.2
	12–11	626.1	31.3	571.9	−1.7	670.7	1.4
$HC_3^{15}N$	9–8	14.1	2.1	12.4	−0.8	14.8	0.4
	10–9	9.0	0.7	8.8	−0.3	9.1	0.1
	11–10	<7	1.4	5.8	3.7	5.0	3.2
	12–11	<5	1.0	3.4	1.0	2.5	0.0
	13–12	<22	4.3	1.8	−0.8	1.1	−1.0

[a]Hyperfine transitions of HC_3N are those of Table A1, starting with the main hf group, followed by the other two hf lines, sorted by increasing frequency.
[b]The adopted uncertainties are at least 5 per cent of the flux. Upper limits are at 5σ. All integrated intensities are in mK km s^{-1}.
[c]$\widetilde{W}$ is the predicted flux based on the models given in Table 2.

This paper has been typeset from a TEX/LATEX file prepared by the author.